

Article

In Situ Electrochemical Impedance Measurements of $\alpha\text{-Fe}_2\text{O}_3$ Nanofibers: Unravelling the Li-Ion Conduction Mechanism in Li-Ion Batteries

Jinhyun Hwang ¹, Dolly Yadav ² , Hang Yang ¹, Injun Jeon ¹, Dingcheng Yang ¹, Jang-Won Seo ¹, Minseung Kang ³, Se-Young Jeong ³ and Chae-Ryong Cho ^{1,2,*} 

¹ Department of Nano Fusion Technology, Pusan National University, Busan 46241, Korea; byjh1005@naver.com (J.H.); 372443279yh@gmail.com (H.Y.); ijeon@pusan.ac.kr (I.J.); dcyang@pusan.ac.kr (D.Y.); str0819@naver.com (J.-W.S.)

² Crystal Bank Research Institute, Pusan National University, Busan 46241, Korea; dolly_yadav61@yahoo.com

³ Department of Nanoenergy Engineering, Pusan National University, Busan 46241, Korea; twomin0000@naver.com (M.K.); syjeong@pusan.ac.kr (S.-Y.J.)

* Correspondence: crcho@pusan.ac.kr; Fax: +82-51-514-2358



Citation: Hwang, J.; Yadav, D.; Yang, H.; Jeon, I.; Yang, D.; Seo, J.-W.; Kang, M.; Jeong, S.-Y.; Cho, C.-R. In Situ Electrochemical Impedance Measurements of $\alpha\text{-Fe}_2\text{O}_3$ Nanofibers: Unravelling the Li-Ion Conduction Mechanism in Li-Ion Batteries. *Batteries* **2022**, *8*, 44. <https://doi.org/10.3390/batteries8050044>

Academic Editor: Catia Arbizzani

Received: 22 March 2022

Accepted: 14 May 2022

Published: 16 May 2022

Publisher's Note: MDPI stays neutral with regard to jurisdictional claims in published maps and institutional affiliations.



Copyright: © 2022 by the authors. Licensee MDPI, Basel, Switzerland. This article is an open access article distributed under the terms and conditions of the Creative Commons Attribution (CC BY) license (<https://creativecommons.org/licenses/by/4.0/>).

Abstract: Unravelling the lithium-ion transport mechanism in $\alpha\text{-Fe}_2\text{O}_3$ nanofibers through in situ electrochemical impedance studies is crucial for realizing their application in high-performance anodes in lithium-ion batteries. Herein, we report the effect of heat treatment conditions on the structure, composition, morphology, and electrochemical properties of $\alpha\text{-Fe}_2\text{O}_3$ nanofibers as an anode for lithium-ion batteries. The $\alpha\text{-Fe}_2\text{O}_3$ nanofibers were synthesized via electrospinning and post-annealing with differences in their annealing temperature of 300, 500, and 700 °C to produce FO300, FO500, and FO700 nanofibers, respectively. Improved electrochemical performance with a high reversible specific capacity of 599.6 mAh g⁻¹ at a current density of 1 A g⁻¹ was achieved after 50 cycles for FO700. The in situ electrochemical impedance spectroscopy studies conducted during the charge/discharge process revealed that the charge transfer and Li-ion diffusion behaviors were related to the crystallinity and structure of the as-synthesized $\alpha\text{-Fe}_2\text{O}_3$ nanofibers. The surfaces of the $\alpha\text{-Fe}_2\text{O}_3$ nanofibers were converted into Fe metal during the charging/discharging process, which resulted in improved electrical conductivity. The electron lifetime, as determined by the time constant of charge transfer, revealed that, when a conversion reaction occurred, the electrons tended to travel through the iron metal in the $\alpha\text{-Fe}_2\text{O}_3$ nanofibers. The role of iron as a pseudo-resistor with negligible capacitance was revealed by charge transfer resistance analysis.

Keywords: Li-ion battery; anode; $\alpha\text{-Fe}_2\text{O}_3$; charge transfer; in situ EIS

1. Introduction

In recent decades, the energy content of energy storage devices has increased continuously, and lithium-ion (Li-ion) batteries have evolved into the best technology for small-scale and large-scale renewable energy applications [1–4]. According to the International Energy Agency (IEA) annual global energy statistics released in 2018, 65% of the world's oil, a representative fossil fuel, is used for transportation and is responsible for the majority of environmental damage [5]. Therefore, transitioning to electric vehicles using commercially available Li-ion batteries may be the fastest solution for reducing air pollution, increasing energy efficiency, and obtaining the most reliable effect for the future development of new and renewable energy. However, graphite (C), which is a negative electrode active material used for currently commercialized Li-ion batteries, has a limited theoretical specific capacity of 372 mAh g⁻¹ and 837 mAh cm⁻³ [6], which is less than the industry requires. Nitrogen- and/or sulfur-doped carbon nanostructures have been widely reported to efficiently improve the electronic properties of carbon materials as an anode [7–9].

One of the most suitable materials for anode-active material that stores lithium through a conversion process is iron oxide ($\alpha\text{-Fe}_2\text{O}_3$), which has a theoretical specific capacity of approximately 1007 mAh g^{-1} and 5331 mAh cm^{-3} [10]. It is also environmentally friendly, has abundant reserves, and has demonstrated technical stability in the sector [6,10]. Although $\alpha\text{-Fe}_2\text{O}_3$ has some drawbacks, such as limited electrical conductivity ($\sim 10^{-10} \text{ S cm}^{-1}$) [11], polarization in the charge/discharge process, and volume change ($\sim 96\%$) occurring from the conversion reaction [12], it can be overcome with a nanostructured design or composite with carbon-based materials [13–20]. The decrease in particle size increases the electrical conductivity, magnetic coercivity, and the usual mechanical and optical properties in a way that matches the wavelengths of electrons, phonons, and magnons [21].

The morphology and composition of iron oxide $\alpha\text{-Fe}_2\text{O}_3$ -based materials fundamentally affect the efficiency of Li-ion migration by reducing the diffusion length, facilitating Li-ion migration [22,23]. The capacity loss based on the irreversibility of the $\text{Li}^+/\alpha\text{-Fe}_2\text{O}_3$ interaction can be minimized by replacing microcrystalline $\alpha\text{-Fe}_2\text{O}_3$ with specific nanoshaped derivatives [24]. Downsizing gives the advantage of a large surface-area-to-volume ratio of nanostructured materials, leading to improved battery performance [24–26]. The $\alpha\text{-Fe}_2\text{O}_3$ of specific topologies such as spherical nanoparticles, nanocubes, nanospindles, nanoflakes, nanowires, nanobelts, nanotubes, nanodiscs, nanocapsules, and nanorods have been explored as anode materials for LIBs [24–29]. Further, composition optimization by incorporating carbon/graphene materials along with the metal oxides also leads to excellent electrical and mechanical properties. When coated on the surface, they improve the excessive formation of the solid-electrolyte interphase (SEI) layer and effectively buffer volume expansion [29].

In addition to the synthesis of improved materials, another important challenge for effective electrode development is determining the fundamental cause of poor electrochemical performance. The cell performance can be evaluated using different physical, electrochemical, and chemical techniques, frequently carried out via *ex situ* analysis. However, to provide in-depth insights into the changes occurring within the cell during operation, *in situ* diagnostic tools have been proposed to acquire information relating to the design, operating parameters, and cell materials [30,31]. Structural analysis and real-time observations during the charge/discharge process confirmed the effect of structural stability on iron oxide using various procedures. Su et al. reported the direct observation of the conversion reaction of Fe_2O_3 /graphene by *in situ* transmission electron microscopy (TEM) [32]. Lee et al. presented structural and microstructural analysis of Fe_2O_3 /reduced graphene oxide by *in situ* X-ray diffraction (XRD) and *in situ* TEM, respectively [33]. However, electrochemical dynamics, such as electron transfer and Li-ion diffusion behavior during the charge/discharge of $\alpha\text{-Fe}_2\text{O}_3$, have received little attention.

In this study, we aimed at inferring the effect of annealing temperature on the structural and the electrochemical performance of $\alpha\text{-Fe}_2\text{O}_3$ nanofibers synthesized at 300, 500, and 700 °C to produce FO300, FO500, and FO700, respectively. The *in situ* electrochemical impedance spectroscopy studies revealed interesting electrochemical behavioral differences in the $\alpha\text{-Fe}_2\text{O}_3$ nanofibers. The FO700 showed excellent capacity retention over FO500 and FO300 owing to its highly crystalline particles with a large and smooth shape. The annealing temperature influenced the crystallite size and the grain boundaries of the synthesized nanofibers. Thereby, in FO500, the formation of smaller-grain-sized Fe_2O_3 particles led to a larger number of grain boundaries, which in turn inhibited charge carrier transport. In FO300, lower annealing temperatures led to the formation of small-grain-sized Fe_2O_3 particles linked via amorphous carbon. The presence of amorphous carbon in the FO300 could also inhibit uniform SEI layer formation on the surface of iron oxide, and in turn reflect its poor Li-ion transport. Hence, we believe that the changes in the Li-ion diffusion behavior and charge transfer during the charge/discharge process analyzed using *in situ* electrochemical impedance spectroscopy (EIS) for $\alpha\text{-Fe}_2\text{O}_3$ synthesized at different annealing temperatures could contribute towards a mechanistic understanding for the development of low-cost, efficient $\alpha\text{-Fe}_2\text{O}_3$ anode materials.

2. Materials and Methods

2.1. Material Synthesis

The $\alpha\text{-Fe}_2\text{O}_3$ nanofibers were synthesized via electrospinning and post-annealing. In a typical process, the precursor solution was prepared by mixing it with 1.4 g of ferric acetylacetone ($\text{Fe}(\text{acac})_3$, 97%, Sigma-Aldrich, St. Louis, MO, USA), 1.6 g of polyvinylpyrrolidone (PVP, $M_w \sim 1,300,000$, Sigma-Aldrich, USA), and 10 mL of N,N-dimethylformamide (DMF, ACS reagent, $\geq 99.8\%$, Sigma-Aldrich, USA). The homogeneous solution was transferred to a 24 mL plastic syringe with a 25-gauge needle tip. A positive voltage of 15 kV was applied between the needle tip and the current collector, leaving a distance of ~ 18 cm. During the electrospinning process, the pumping rate of the precursor solution, the temperature, and the humidity were maintained at 1.0 mL h^{-1} , 25°C , and 35%, respectively. The as-spun polymeric nanofibers were dried at 100°C for 12 h in a vacuum to remove any remaining DMF solvent, and $\alpha\text{-Fe}_2\text{O}_3$ nanofibers were then obtained by post-annealing at different annealing temperatures of 300, 500, and 700°C for 3 h with a heating rate of 2°C min^{-1} in air (denoted as FO300, FO500, and FO700), respectively.

2.2. Material Characterization

The crystallinity of the $\alpha\text{-Fe}_2\text{O}_3$ nanofibers was characterized by XRD (Malvern Instruments, United Kingdom, X'Pert³ Powder, Cu-K α radiation, $\lambda = 1.5406 \text{ \AA}$) in the angle range of $20\text{--}80^\circ$. A Raman spectrometer (PSU-III FDA, CNI Optoelectronics Tech. Co, Ltd., Changchun, China) with a 532 nm laser as the excitation source from 300 to 2550 cm^{-1} was used. The morphologies of the samples were investigated using field-emission scanning electron microscopy (SEM, Hitachi, Tokyo, Japan, S4700). The chemical bonding states of the samples were determined using X-ray photoelectron spectroscopy (XPS) using a commercial unit (K-Alpha⁺, Thermo Fisher Scientific, Waltham, MA, USA) equipped with a multichannel detector in the range of 0–1200 eV using monochromatic Al K α radiation (1486.6 eV). The carbon content and thermal stability of the samples were measured through thermogravimetric analysis (TGA; DTG-60H, Shimadzu, Tokyo, Japan) at a heating rate of $10^\circ\text{C min}^{-1}$.

2.3. Electrochemical Measurements

The working electrodes were prepared by mixing $\alpha\text{-Fe}_2\text{O}_3$ nanofibers, acetylene black, and carboxymethyl cellulose (deionized water as solvent) at a weight ratio of 80:10:10. The mass loading of active materials in the electrode was $1.8\text{--}2.1 \text{ mg cm}^{-2}$ (electrode loading level = $2.25\text{--}2.6 \text{ mg cm}^{-2}$). The slurry was coated on Cu foil using a doctor blade, dried at 60°C in a vacuum oven, and punched into a $\phi 14 \text{ mm}$ disk. To evaluate the electrochemical performance of the $\alpha\text{-Fe}_2\text{O}_3$ nanofibers, a CR2032 coin cell was assembled in a glove box. The active material was used as the working electrode, Li metal as the counter electrode, and 1 M LiPF₆ dissolved in a mixture of ethyl carbonate and diethyl carbonate (1:1, vol%) with 10 wt.% fluoroethylene carbonate as the electrolyte. Galvanostatic charge/discharge cycling profiles were obtained using an automatic battery test system (WBCS 3000, Wonatech, Korea). EIS was performed using a multichannel impedance analyzer (ZIVE MP1, Wonatech, Korea) in a frequency range of 100 kHz to 0.1 Hz with an AC signal of 10 mV amplitude. Based on the conversion reaction of metal oxide, to investigate the Li-ion diffusion and charge transfer behavior of the $\alpha\text{-Fe}_2\text{O}_3$ nanofibers during the charge/discharge process, *in situ* EIS measurements were performed at 3, 2, 1.5, 1, 0.5, and 0.01 V (denoted as D3.0–D0.01, respectively) during discharge and 0.5, 1, 1.5, and 2 V (denoted as C0.5–C2.0, respectively) during charge.

3. Results and Discussion

Figure 1 shows the SEM images of as-spun polymeric nanofibers and $\alpha\text{-Fe}_2\text{O}_3$ nanofibers annealed at 300, 500, and 700°C , respectively. The morphologies of the as-spun polymeric nanofibers showed a uniform shape and size, with a diameter of 580 nm and a smooth surface (Figure 1a,b). As the annealing temperature was increased, the PVP, a thermoplastic

polymer, changed its shape easily and was decomposed by O_2 to CO_2 , forming pores inside. As a result, the α - Fe_2O_3 obtained at 300 °C (FO300) showed a uniform shape and showed hollow nanofibers with a diameter of 290 nm, composed of small crystalline α - Fe_2O_3 particles connected by amorphous carbon (Figure 1c,d). As the temperature was increased to 500 °C, the Fe^{3+} and O^{2-} migration and rearrangement was accelerated, leading to the formation of defects and pores in the FO500 nanofibers and resulting in a decrease in diameter to 231 nm (Figure 1e,f). When the temperature was further increased to 700 °C, the nanofibers became smaller, with cured pores, a much smoother surface with a diameter of 176 nm, and highly crystalline grains (Figure 1g,h). It could be expected that the complete rearrangement of Fe^{3+} and O^{2-} at a higher temperature occurred, leading to the formation of smoother, finer, and more stabilized structured nanofibers [34]. The as-synthesized nanofibers with their diameters are depicted in Figure S1 (Supplementary Materials). The SEM/EDS analysis of FO300, FO500, and FO700 (Figure S2) showed uniform distribution of the elements (Fe and O) in the α - Fe_2O_3 nanofibers. It is noteworthy that the FO700 sample (Figure S2l,m) exhibited a higher amount of iron and oxygen, compared to the FO500 (Figure S2g,h) and the FO300 samples (Figure S2b,c). This was due to the complete oxidation of α - Fe_2O_3 nanofibers at 700 °C, resulting in the formation of uniform Fe_2O_3 -rich nanofibers.

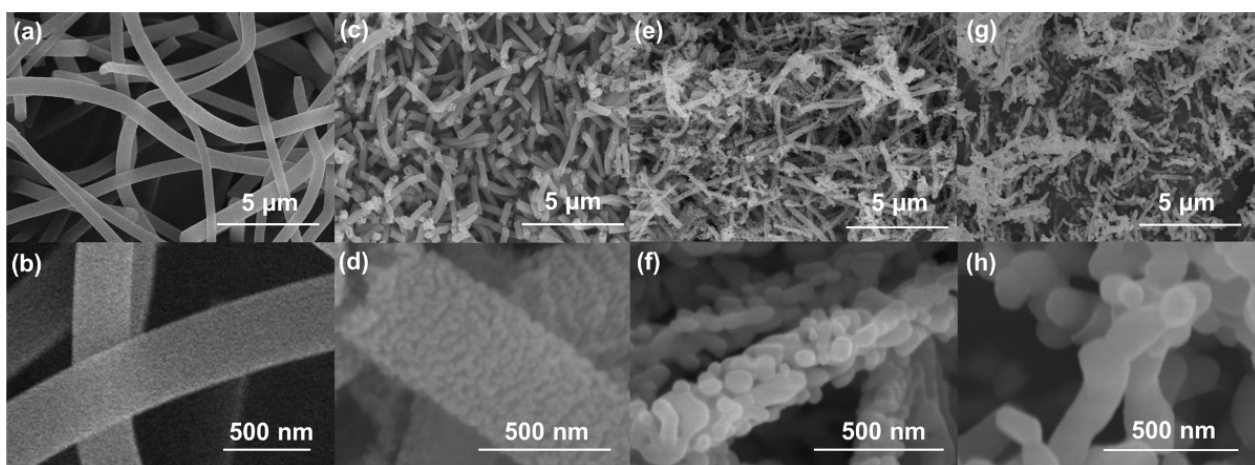


Figure 1. SEM surface images of (a,b) as-spun polymeric nanofibers and α - Fe_2O_3 nanofibers annealed at (c,d) 300 °C, (e,f) 500 °C, and (g,h) 700 °C.

Figure 2 shows the XRD patterns and Raman spectra of the α - Fe_2O_3 nanofibers. Figure 2a shows the XRD patterns of α - Fe_2O_3 nanofibers annealed at different temperatures. The well-defined diffraction peaks of FO500 and FO700 indicate the hexagonal structure of hematite (ICSD No. 98-006-6756) in the R-3c space group, with peaks at 33.2°, 35.6°, 40.8°, 49.5°, 54.1°, 62.5°, and 64.0°, corresponding to the (104), (110), (113), (024), (116), (214), and (030) planes, and no secondary phase was observed. As the annealing temperature increased, the crystallinity increased, and the full width at half maximum of the peaks decreased [35]. The very weak intensity of the diffraction peak of FO300 indicates that the as-spun nanofiber (Fe salt + PVP) was not completely crystallized and remained in the dominant amorphous phase at 300 °C. Residual PVP with amorphous carbon also caused a broad peak in the range of 20–40°. The XRD data were also used to predict the crystallite size, where a peak broadening technique was applied using the Scherrer equation for particle size calculations. The average crystallite sizes of FO300, FO500, and FO700 were calculated as 17.05 nm, 29.54 nm, and 37.38 nm (Figure S3). The increase in the average crystallite size with the increase in the annealing temperature was suggestive of the complete oxidation of the α - Fe_2O_3 nanofibers, resulting in an increase in crystallinity and thereby an increase in conductivity.

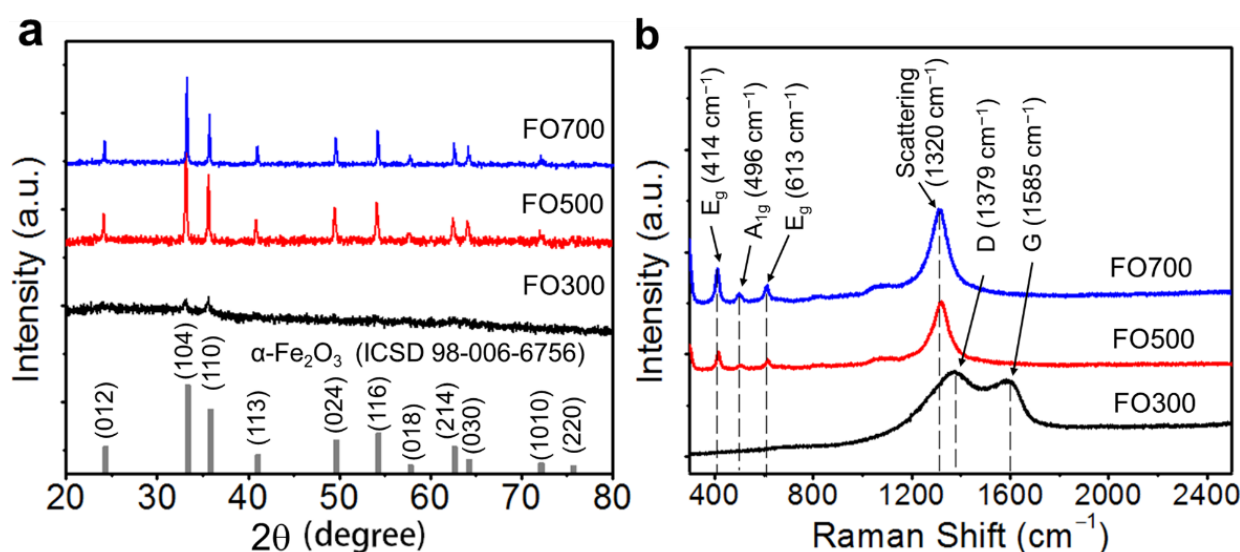


Figure 2. (a) XRD patterns and (b) Raman spectra of the $\alpha\text{-Fe}_2\text{O}_3$ nanofibers annealed at 300, 500, and 700 °C, denoted as FO300, FO500, and FO700, respectively.

Figure 2b shows the Raman spectra related to the molecular vibration of the structure including carbon. In the FO300 sample, a D-mode and G-mode at approximately 1379 and 1585 cm⁻¹ can be observed, respectively, which indicates the existence of carbon, which is consistent with the XRD results. E_g modes at 414 and 613 cm⁻¹, an A_{1g} mode at 496 cm⁻¹, and two magnon scattering modes at 1320 cm⁻¹ were observed in the FO500 and FO700 samples [36]. A broad peak at 1080 cm⁻¹, related to the high crystallinity of $\alpha\text{-Fe}_2\text{O}_3$, was also observed [37]. Each mode shifted slightly to a lower wavenumber owing to the material defects and surface bonding. The chemical bonding and the composition were further confirmed by the X-ray photoelectron spectroscopy (XPS) analysis of FO300, FO500, and FO700 (Figures S4–S6), revealing their compositional and chemical bonding states. The survey-scan analysis for all of the nanofibers is shown in Figure S4. As expected, the presence of C 1s, along with O 1s, N 1s, and Fe 2p peaks, was observed in FO300. In Figures S4 and S5, in the narrow scan of each element, two sharp peaks with binding energies of 711 and 724 eV were observed, and these correspond to $\text{Fe}^{3+}\text{2p}_{2/3}$ and $\text{Fe}^{3+}\text{2p}_{1/2}$, respectively. Large and broader satellite peaks at 716 and 730 eV were also observed, which are characteristic of $\alpha\text{-Fe}_2\text{O}_3$ [38,39]. As the annealing temperature increased, the peak intensities of carbon and nitrogen quickly decreased owing to the decomposition by the chemical reaction. The presence of Fe metal was also observed in the XPS deconvoluted spectrum at Fe 2p at 708.13 eV in the FO300 nanofibers (Figure S5a). It is expected that, due to the presence of a large amount of carbon in the Fe_2O_3 nanofiber matrix in FO300, the formation of Fe metal occurred during annealing in an air atmosphere at 300 °C by the following equation: $\text{FeO}_x(\text{s}) + x\text{C}(\text{s}) \rightarrow \text{Fe}(\text{s}) + x\text{CO}(\text{g})$ [40]. The carbon content in the Fe_2O_3 nanofibers was also calculated on the basis of their thermogravimetric (TGA) weight loss profiles (Figure S7a,b). The carbon content in FO700 was expected to be the lowest owing to the estimated carbon content in the as-spun, FO300, and FO500 nanofibers, found to be 84.5%, 8.3%, and 0.3%, respectively. The correlation between the TGA, XPS, and EDS successfully proved the structure and composition of all of the $\alpha\text{-Fe}_2\text{O}_3$ nanofibers.

The electrochemical performance in terms of the reversibility and rate capability of the $\alpha\text{-Fe}_2\text{O}_3$ nanofibers was evaluated using a galvanostatic charge/discharge process (Figure 3). As shown in Figure 3a, the charge/discharge process was performed during the initial five cycles with a current density of 0.1 A g⁻¹ for stable SEI formation, and it was subsequently tested at 1 A g⁻¹. After 50 cycles, the discharge capacity of FO700 remained at 600 mAh g⁻¹, which was better than the 236 mAh g⁻¹ of FO500. This can be attributed

to the lower crystallinity of FO500. Although the initial capacity of the porous FO500 in the first several cycles was higher than that of other samples, it decreased rapidly as the fiber morphology was changed more easily owing to the conversion reaction of the sample [41] (Figure S11). Although FO300 showed a better first discharge specific capacity, it decreased rapidly from 1167 to 380 mAh g^{-1} , which can be attributed to the low crystallinity of $\alpha\text{-Fe}_2\text{O}_3$ and the carbon defects [42,43].

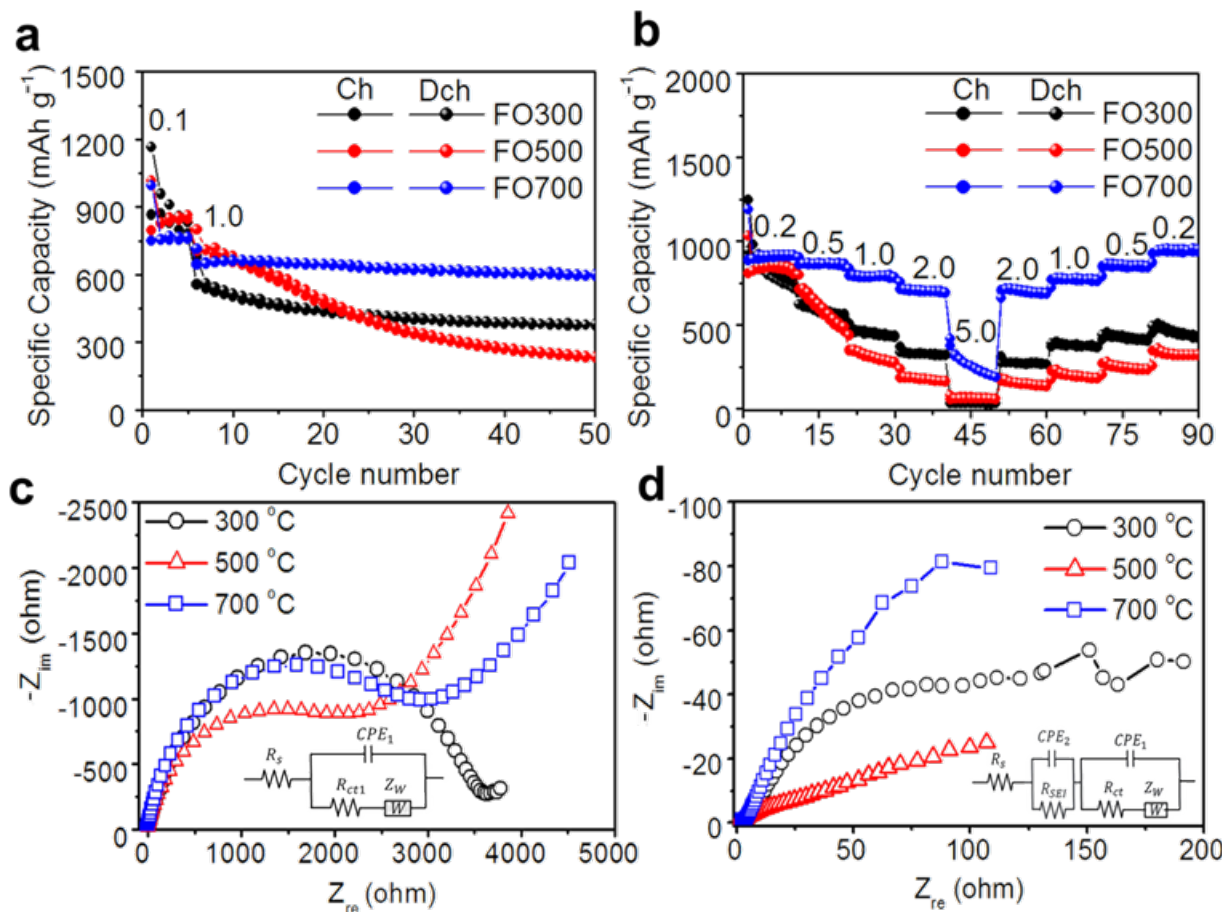


Figure 3. Electrochemical performance for the $\alpha\text{-Fe}_2\text{O}_3$ nanofibers: (a) the cycle stability at a current density of 1.0 A g^{-1} , (b) the rate capability at various current densities, and the Nyquist plots of the $\alpha\text{-Fe}_2\text{O}_3$ nanofibers (c) before and (d) after cycling (the insets in Figure 3c,d show equivalent circuits used for fitting).

The CV profiles of the FO500 and FO700 $\alpha\text{-Fe}_2\text{O}_3$ nanofibers for the initial three cycles were recorded in the potential window of $0.01\text{--}3.0 \text{ V}$ at a scan rate of 0.1 mV s^{-1} (Figure S8). The CV profile shows a strong reduction peak at 0.75 V , and it decreases upon successive cycles due to the irreversible formation of the SEI layer. The decomposition of electrolytes at the interface resulted in the formation of the SEI film, where the Li-ions embedded into the Fe_2O_3 crystal structure formed into $\text{Li}_x\text{Fe}_2\text{O}_3$ [44]. On the other hand, the distinct oxidation peaks observed at approximately 1.4 and 1.7 V can be attributed to the reversible multistep oxidation of $\text{Fe}(0)$ to FeO and Fe_2O_3 , respectively [45–47]. In Figure S8a, we can observe a shift in the peak position during the second and third cycles in FO500, which could be due to the attenuation of capacity and the collapse of the iron oxide structure during cycling [48]. On the other hand, FO700 (Figure S8b) showed good overlap in the last two cycles, demonstrating the better stability of FO700 as an anode material than FO500 [34]. The CV of FO300 (Figure S8c) showed very poor conductivity, which could be expected due to the presence of amorphous carbon, which might lead to poor conductivity and other side reactions during cycling [49].

Concerning the rate capability shown in Figure 3b, FO700 had better rate performance of 933, 871, 796, and 710 mAh g⁻¹ at current densities of 0.2, 0.5, 1, and 2 A g⁻¹, respectively, and 261 mAh g⁻¹ at the much higher current density of 5 A g⁻¹. However, FO300 delivered lower specific discharge capacities of 878, 603, 458, 332, and 31 mAh g⁻¹ at the same current densities compared with those of FO700. In particular, it did not show any significant improvement at high current densities, such as 5 A g⁻¹, so it is considered that the structural linkage effect was obtained by carbon. FO500 showed a significant specific capacity of 865 mAh g⁻¹ at 0.2 A g⁻¹, but it rapidly decreased as the current density increased. Furthermore, owing to changes in morphology and crystallinity, the capacity could not recover to its original high capacity when reverting to low current densities (Figure S11). However, FO700 not only had a high specific capacity even at a high current density but also had a high capability of recovering to the initial value. The EIS data of the samples are presented as Nyquist plots and equivalent circuit models in Figure 3c,d. When studying the electrochemical system of an anode using EIS, an equivalent circuit that consists of resistance (R), capacitance (C), inductance (L), and other elements coupled in series or in parallel is used. The values of these parameters can be determined quantitatively by fitting the EIS measurement data, and the electrochemical meaning of each parameter can be assigned. In a Li-ion battery half-cell system, R, the constant-phase element (CPE) and the Warburg impedance (Z_w) are included, as shown in the insets of Figure 3c,d, where R_s is the bulk resistance related to the electrolyte, electrode surface, current collector, and separator corresponding to ohmic loss, and R_{ct} represents the charge transfer resistance associated with the electrochemical reaction kinetics in the intermediate-frequency region. CPE₁ and CPE₂ are the constant-phase elements that account for the depressed semicircle in the experimental spectra resulting from the charge transfer and the interfacial layer resistance after the cycling experiments [50–52]. R_{SEI} is the interfacial layer resistance after cycling in the high-frequency region. Furthermore, Z_w is the impedance caused by the diffusion behavior of Li-ions in the low-frequency region, and the diffusion resistance (R_w) and diffusion capacitor (C_w) can be regarded as configured in series.

The diffusion coefficient, D_{Li^+} , is calculated by fitting the EIS data using equivalent circuit models and the following equations:

$$Z_{re} = R_s + R_{SEI} + R_{ct} + \sigma\omega^{-1/2}, \quad (1)$$

$$D_{Li^+} = R^2 T^2 / 2A^2 n^4 F^4 C_{Li^+}^2 \sigma^2, \quad (2)$$

where R is the gas constant (8.314 J mol⁻¹ K⁻¹), T is the absolute temperature, A is the surface area of the electrode, n is the number of transfer electrons per molecule of material involved in the reaction, F is the Faraday constant (96,485 C mol⁻¹), C_{Li^+} is the Li-ion concentration, and σ is the Warburg coefficient calculated from the relationship between Z_{re} and the reciprocal square root of the angular frequency ($\omega^{-1/2}$). Based on the equivalent circuit model, the R_s , R_{SEI} , R_{ct} , σ , and D_{Li^+} values of the α -Fe₂O₃ nanofibers annealed at different temperatures were calculated using Equations (1) and (2) and are listed in Table 1.

Table 1. Calculated resistances (R_s , R_{SEI} , and R_{ct}), Warburg coefficient (σ), and diffusion coefficient (D_{Li^+}) from the Nyquist plots and Equations (1) and (2).

	Samples	R_s (Ω)	R_{SEI} (Ω)	R_{ct} (Ω)	σ (Ω s ^{-1/2})	D_{Li^+} (cm ² s ⁻¹)
Before cycling	FO300	2.11	-	3.42×10^3	306	2.39×10^{-18}
	FO500	2.36	-	2.00×10^3	103	3.95×10^{-19}
	FO700	2.51	-	2.57×10^3	822	3.30×10^{-19}
After 50 cycles	FO300	2.29	2.62	114	50.0	3.24×10^{-17}
	FO500	2.45	2.94	267	83.0	3.24×10^{-17}
	FO700	2.63	1.41	108	37.5	1.59×10^{-16}

Before cycling, FO500 exhibited a lower R_{ct} than the other two samples because the porous structure had greater electrolyte contact with the electrode material and shorter

pathways for lithiation and delithiation, resulting in a higher initial capacity (Figure 3c). After cycling, FO700 exhibited a high charge transfer resistance of $108\ \Omega$, and FO300 exhibited an improved R_{ct} of $114\ \Omega$, compared with the $267\ \Omega$ of FO500. This was highly correlated with the morphological changes in FO500 and the internal pathway generated by the structural linkage with carbon in FO300 (Table 1). The high crystallinity and connection with the nanofibers facilitated the movement of Li-ions and electrons, further improving the conduction properties. The conduction of Li-ions and electrons depends on the composition of the electrode materials. All of the samples showed high σ values before cycling, but the σ values decreased rapidly after cycling. FO700 showed the lowest σ value, indicating faster and more efficient Li-ion diffusion. Similar to the interpretation of charge transfer, the D_{Li^+} values of FO700 were $1.59 \times 10^{-16}\ cm^2\ s^{-1}$ higher than the 8.94×10^{-16} and $3.24 \times 10^{-16}\ cm^2\ s^{-1}$ values of FO300 and FO500, respectively. This also indicates that high crystallinity and a stable nanofiber structure improve the diffusion of Li-ions.

EIS analysis before and after cycling indicates that the presence of carbon and the high crystallinity of $\alpha\text{-Fe}_2\text{O}_3$ are favorable for the diffusion of Li-ions; however, there are limitations in investigating the electrochemical dynamics in the charging/discharging process. Figure 4 shows the in situ EIS Nyquist plots of the $\alpha\text{-Fe}_2\text{O}_3$ nanofibers at various voltages, from 1.5 V upon discharge to 1.5 V upon charge (denoted as D1.5–C1.5). In the first cycle, irreversible reactions were included by the decomposition of the electrolyte and formation of the SEI layer, and the semicircle corresponding to R_{ct} and R_{SEI} showed relatively large values. The shape of the semicircle then changed with a certain pattern in each voltage region, where the semicircle became larger with discharging and smaller with charging. A schematic of the conversion reaction and corresponding equivalent circuit models of the Fe_2O_3 nanofiber during charging and discharging is shown in Figure S9.

Figure 5 shows the calculated electrochemical parameters at each voltage. In the initial three cycles, R_s and R_{SEI} increased owing to the formation of the SEI layer during discharging and decreased owing to the partial reduction and the decomposition of the SEI layer during charging [53]. After the first cycle, the values were constant, indicating that the bulk region and SEI layer had stabilized. The relaxation time [54], τ , also called the electron lifetime [55] or time constant [56], is the time required to reach a specific region where an AC-type signal is observed in EIS, and this is important location information. The relationship of frequency, resistance, and capacitance can be calculated using the following equation.

$$\tau = RC = 1/f_{max}, \quad (3)$$

where f_{max} is the maximum peak frequency in the Bode plot. τ_{ct} denotes the time required for the charge to reach the position where the charge transfer occurs. In this study, it is the conversion reaction between the electrode material and Li-ions in the electrolyte. According to general chemical reaction kinetics, a lower rate of Li-ions determines the overall rate of the system. However, the average frequency range of τ_{ct} is approximately 10 kHz, which is the region where the movement of Li-ions is restricted and the movement of electrons is observed in the EIS analysis [57–60]. In addition, in terms of electron lifetime, the metal oxide is mainly affected by electrons, owing to its low electrical conductivity. Bisquert et al. showed that the electron lifetime can be calculated using RC circuits in dye-sensitized solar cells [61]. When the resistance R and the capacitance C from the semicircle of R_{ct} and CPE are the respective constant-phase elements that account for the depressed semicircle in the experimental spectra, calculated by data fitting [50], the charge/discharge cycle is divided into two sections: the “no conversion section” (NCS; D3.0–D1.5/C1.5–C3.0) and the “conversion section” (CS; D1.5–C1.5).

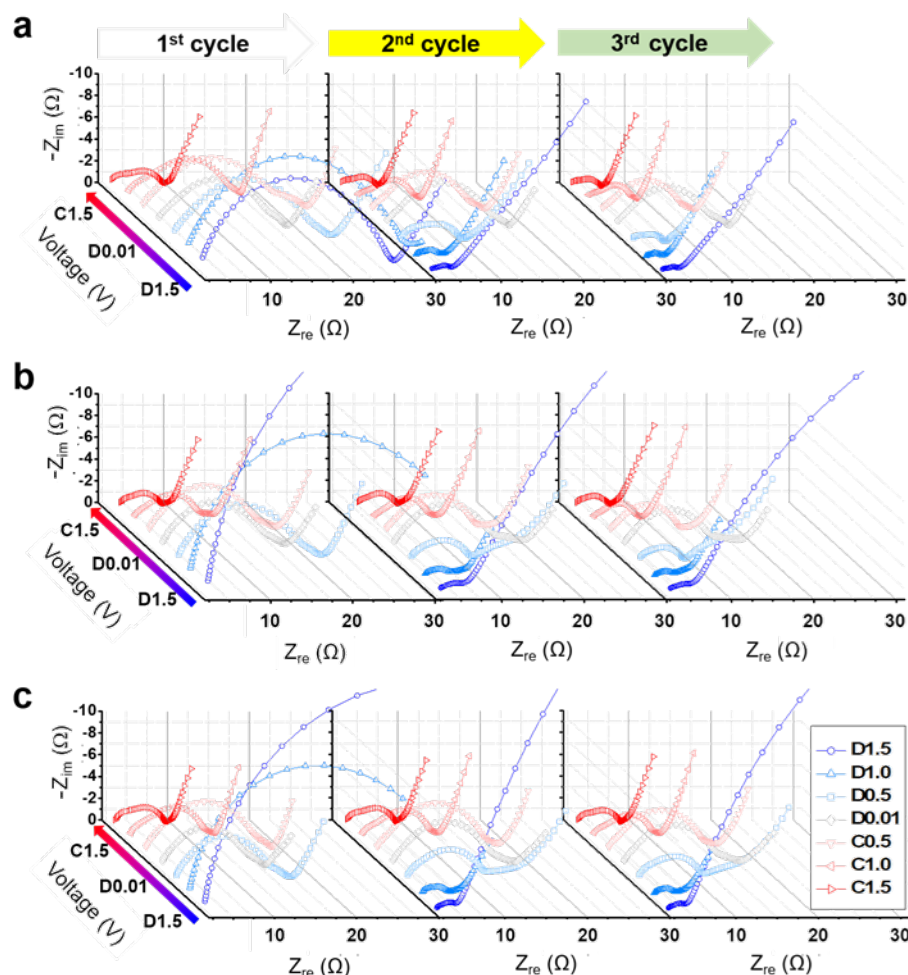


Figure 4. Nyquist plots of $\alpha\text{-Fe}_2\text{O}_3$ nanofibers at various voltages from D1.5 to C1.5: the $\alpha\text{-Fe}_2\text{O}_3$ nanofibers were annealed at (a) 300 $^{\circ}\text{C}$, (b) 500 $^{\circ}\text{C}$, and (c) 700 $^{\circ}\text{C}$.

The τ_{ct} in the CS decreased compared with that in the NCS, indicating a shortened electron lifetime. This result shows that electrons are easily trapped in the region separated by the Fe metal and Li_2O . The R_{ct} and D_{Li^+} were also clearly distinguished in NCS and CS. The R_{ct} had a high charge transfer resistance at D3.0 and decreased rapidly at D1.5. This shows that, even if the electrons survive for a long time, the magnitude of the charge transfer resistance is large in $\alpha\text{-Fe}_2\text{O}_3$. It also shows that the magnitude of the charge transfer resistance decreases, even though the conversion reaction is initiated and electrons are trapped by Li_2O and Fe. This is because the total charge transfer resistance is affected by the composition of the transfer subject. When a conversion reaction occurs, the electron can choose a shortcut for electron transfer—that is, an electrical path through the Fe. Interestingly, FO300, a carbon-containing $\alpha\text{-Fe}_2\text{O}_3$, also had small R_{ct} values in the NCS region, indicating that carbon connected the oxide particles, so electron transport was favorable and effective. However, when the conversion reaction occurred, the R_{ct} values of FO500 and FO700 were similar. This proves that there is no contribution of carbon because the electrons choose the electrical path through the Fe. At D0.01, when the conversion reaction was complete, R_{ct} decreased slightly. Previous studies have shown that the larger the size of the Li_2O , the greater the electrochemical inactivation, leading to a decrease in capacity [62]. The D_{Li^+} increases in the CS with respect to Li-ion diffusion. This result can be explained by the effect of the concentration difference in the electric double layer. In the NCS, the charge was in a completely separated state, in which almost no oxidation-reduction reaction occurred. Therefore, it is difficult to make a concentration difference in the electric double layer, thereby reducing the diffusion rate [63]. When a conversion

reaction occurred, the Li-ion concentration and diffusion rate increased. In addition, when promoting Li-ion diffusion, the selection of diffusion pathways increased, thereby facilitating the recombination of electrons and Li-ions.

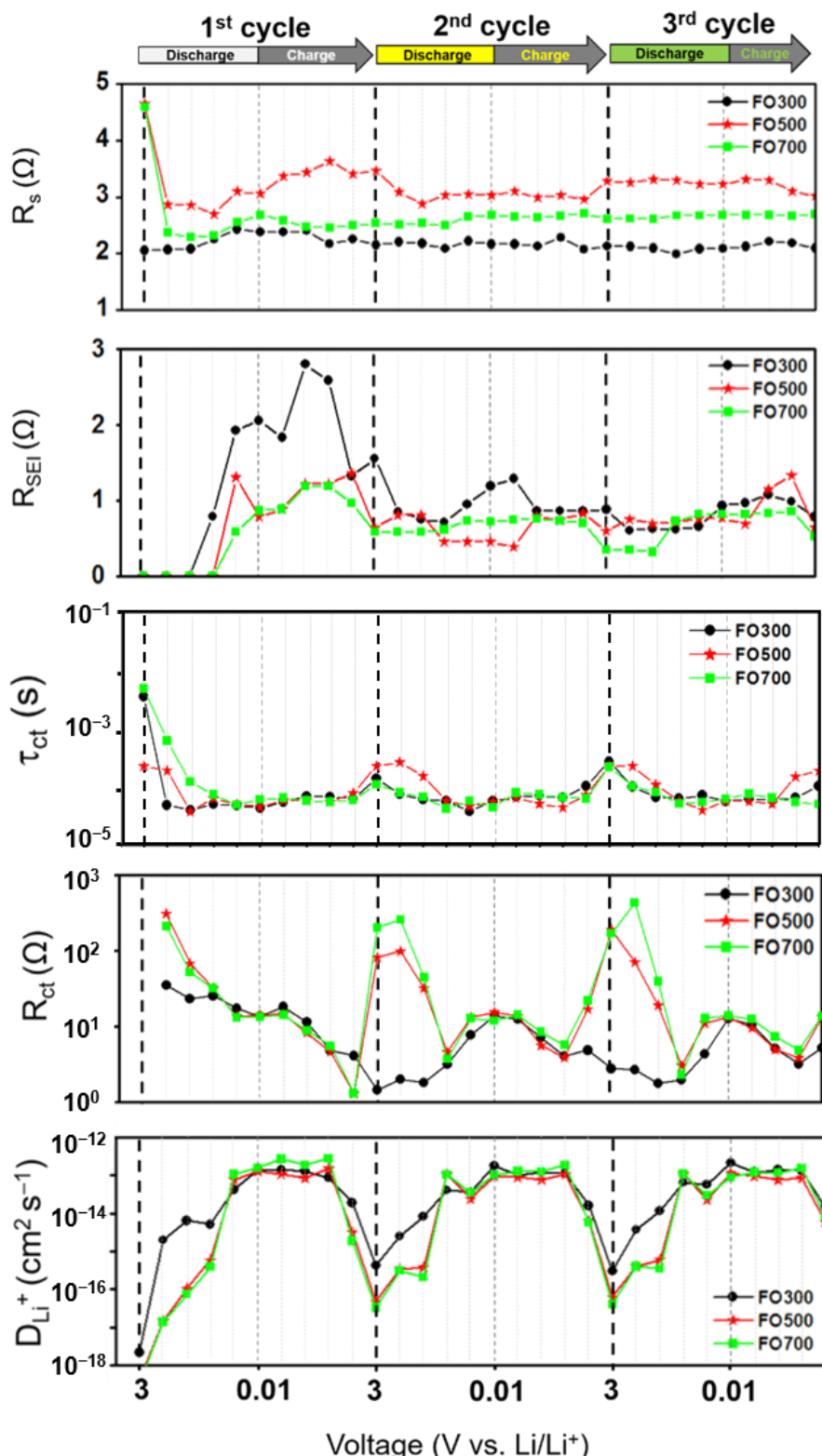


Figure 5. Parameters (R_s , R_{SEI} , R_{ct} , τ_{ct} , and D_{Li^+}) obtained by fitting and calculation using equivalent circuits and Equations (1)–(3) at each voltage: the $\alpha\text{-Fe}_2\text{O}_3$ nanofibers were annealed at 300, 500, and 700 °C.

For a more detailed analysis of the charge transfer reactions, it was inferred that each material had different charge transfer properties (Figure 6). Each semicircle corresponds to a material according to the frequency. The order is $\alpha\text{-Fe}_2\text{O}_3$, Li_2O , and Fe, and real-time structural analysis shows that Fe particles exist inside the Li_2O matrix in a completely discharged state [30]. Figure 6a–c show the charge transfer resistances (R_{ct1} , R_{ct2} , and R_{ct3}) calculated from R_{ct} at each voltage. Figure S10 shows the EIS data of the electrodes and the equivalent circuit parameters used to calculate R_{ct1} , R_{ct2} , and R_{ct3} . In the initial three cycles, there was no clear phase separation because of the irreversible reaction with the electrolyte; however, after the second cycle, R_{ct1} , R_{ct2} , and R_{ct3} were observed in the CS. These resistances were arranged in the order of R_{ct2} , R_{ct1} , and R_{ct3} , which is consistent with the electrically conductive properties of Li_2O , $\alpha\text{-Fe}_2\text{O}_3$, and Fe. R_{ct1} and R_{ct2} tended to be inverted according to the voltage response section. This property can be attributed to the change in the diffusion characteristics caused by the involvement of Li-ions in addition to electrons. In the case of FO300, the contribution of carbon to R_{ct1} was included, there was no significant change in the overall reaction, and Li_2O provided the main resistance during the conversion reaction. In particular, as the discharging process progressed, it increased from 0.42 to 9.57 Ω , and the increase in Li_2O was considered to be the main cause of the electrical short circuit. In addition, the R_{ct3} values of FO500 with low crystallinity were 6.10 and 3.67 Ω , which were higher than the 1.91 and 2.12 Ω of FO700, suggesting that Fe also had defects inside. The FO500 had a higher R_{ct3} of 6.10 and 3.67 Ω compared with the FO700, which had values of 1.91 and 2.12 Ω because of the presence of defects inside the Fe of the FO500. The values of R_{ct1} , R_{ct2} , and R_{ct3} in various states are summarized in Table S1.

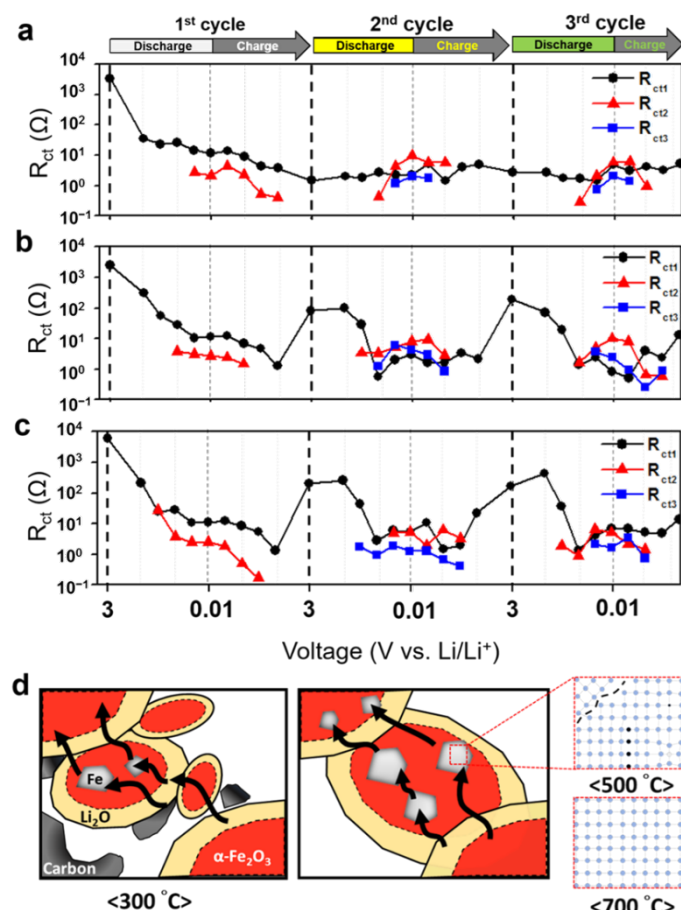


Figure 6. Calculated R_{ct1} , R_{ct2} , and R_{ct3} at each voltage by separation of charge transfer resistance of (a) FO300, (b) FO500, and (c) FO700; (d) schematic diagram of the electrical path in $\alpha\text{-Fe}_2\text{O}_3$ nanofibers.

Figure 6d is a schematic diagram of the electrical pathway during the conversion reaction. When electrons migrated during the conversion reaction, they had to pass through the outer interface and inner crystals of the $\alpha\text{-Fe}_2\text{O}_3$, Li_2O , and Fe. Low crystallinity caused the outer interface to become irregular and changed the internal crystal orientation along with the defects. It then limited the movement of electrons to pass through the grains; as a result, the Fe in FO500 had a large charge transfer resistance with low electrical conductivity. At the same time, from the different shape of the semicircle corresponding to the charge transfer region of the Nyquist plot, it can be concluded that the change in components affected the charge transfer path and limited the Li-ion storage location. In FO500 and FO700, a very low slope or flat impedance values were observed before the diffusion region in the low-frequency region. These values indicate that the electric double layer did not form because there was almost no capacitance, and there was an element that provided resistance to the charge transfer or diffusion process. This factor was considered to be related to Fe according to the separation analysis result of the charge transfer resistance. In addition, the three-dimensionally immersed Fe acted as a pseudo-resistive circuit, indicating that it was ineffective for Li-ion diffusion.

4. Conclusions

The electrochemical dynamics of Li-ions in $\alpha\text{-Fe}_2\text{O}_3$ nanofibers during charge and discharge were investigated. The effect of chemical composition on the charge transfer and Li-ion diffusion behavior of $\alpha\text{-Fe}_2\text{O}_3$ nanofibers synthesized at different annealing temperatures was studied. The resistance components and Li-ion diffusion coefficient were obtained for each voltage segment in the initial three cycles using in situ EIS. The electron transfer and Li-ion diffusion processes were analyzed based on their structural characteristics, such as changes in the composition of $\alpha\text{-Fe}_2\text{O}_3$ nanofibers, the presence or absence of carbon, and crystallinity, where the conversion reaction may or may not occur. The electrical path through the Fe was chosen when the conversion reaction occurred, where the electron lifetime is denoted by τ_{ct} . The annealing temperature influenced the crystallite size and hence the grain boundaries of the synthesized nanofibers. The FO700 showed excellent capacity retention over FO500 and FO300 owing to its highly crystalline and larger-grain-size smooth-surface nanofibers. On the other hand, FO500 showed the formation of smaller-grain-size Fe_2O_3 particles with a larger number of grain boundaries, which in turn could inhibit their charge carrier transport, leading to poor performance. Owing to the presence of carbon in FO300, it was electrically connected, so no conversion reaction occurred, supporting electron transfer and Li-ion diffusion. However, the poor SEI formation on the surface of iron oxide could be one of the reasons for the poor electrochemical performance in FO300. Based on the separation analysis of the charge transfer resistance, whether the Fe formed during complete discharge acts as a pseudo-resistive element with low capacitance, thereby reducing the dynamic characteristics of the battery, was investigated. Additionally, it was found that, when the crystallinity of $\alpha\text{-Fe}_2\text{O}_3$ is poor, defects may be included in the conversion reaction to Fe, lowering the electrical conductivity. Conclusively, the present work provides insight on the structure and phase changes occurring in $\alpha\text{-Fe}_2\text{O}_3$ conversion-type anode material through in situ impedance measurements, which is a step towards the use of their electrochemical performance for Li-ion batteries with a higher energy storage.

Supplementary Materials: The following supporting materials can be downloaded at: <https://www.mdpi.com/article/10.3390/batteries8050044/s1>; Figure S1: (a) Pictorial presentation and (b) the average diameter of the nanofibers calculated from the SEM images; Figure S2: SEM and EDS elemental mapping images of the samples (a–e) FO300, (f–j) FO500 and (k–o) FO700; Figure S3: Graphical presentation of average crystallite size of the FO300, FO500 and FO700 calculated from XRD data; Figure S4: XPS survey analysis for FO300, FO500 and FO700; Figure S5: XPS narrow-scan spectra of (a) Fe 2p, (b) O 1s and (c) C 1s for FO300, FO500 and FO700; Figure S6: XPS narrow-scan spectrum of N 1s for FO300; Figure S7: (a) TGA analysis and (b) carbon content calculated on the basis of weight loss % from TGA data for as-spun, FO300 and FO500. Carbon content of FO700

was not detected (around 0.1 wt%, not shown TGA data); Figure S8: Cyclic voltammograms of (a) FO500, (b) FO700, and (c) FO300 at a scan rate of 0.1 mV s^{-1} ; Figure S9: Schematic of the conversion reaction and corresponding equivalent circuit models for the samples during charge/discharge process; Figure S10: (a–c) EIS data (black color: FO300, red color: FO500 and blue color: FO700) and (d) equivalent circuit used to calculate R_{ct1} , R_{ct2} and R_{ct3} parameters represented in the Figure 6 during second cycle; Figure S11: SEM images of FO500 (a) before and (b) after cycling experiments; Table S1: The charge transfer resistances calculated for three cycles for FO300, FO500 and FO700.

Author Contributions: J.H. and D.Y. (Dolly Yadav) contributed equally to this study. J.H. contributed to conceptualization, experiments, characterization, and manuscript writing. D.Y. (Dolly Yadav) and H.Y. performed analysis, experimental investigation, manuscript writing, and revision. I.J., D.Y. (Dingcheng Yang) and J.-W.S. performed formal data analysis and manuscript preparation. S.-Y.J. and M.K. contributed to formal analysis. C.-R.C. performed supervision, project administration, experimental planning, manuscript preparation, and funding acquisition. All authors have read and agreed to the published version of the manuscript.

Funding: This research was supported by the National Research Foundation of Korea (NRF) funded by the MSIT and MEST (grant numbers NRF-2021R1A4A1022198, NRF-2019R1A2C1009889, and NRF-2018R1A5A1025594).

Institutional Review Board Statement: Not applicable.

Informed Consent Statement: Not applicable.

Data Availability Statement: The data presented in this study are available from the corresponding author on request.

Conflicts of Interest: The authors declare that there is no conflict of interest.

References

- Grey, C.P.; Hall, D.S. Prospects for lithium-ion batteries and beyond—A 2030 vision. *Nat. Commun.* **2020**, *11*, 6279. [[CrossRef](#)]
- Bresser, D.; Passerini, S.; Scrosati, B. Leveraging valuable synergies by combining alloying and conversion for lithium-ion anodes. *Energy Environ. Sci.* **2016**, *9*, 3348–3367. [[CrossRef](#)]
- Tian, Y.; Zeng, G.; Rutt, A.; Shi, T.; Kim, H.; Wang, J.; Koettgen, J.; Sun, Y.; Ouyang, B.; Chen, T.; et al. Promises and challenges of next-generation “Beyond Li-ion” batteries for electric vehicles and grid decarbonization. *Chem. Rev.* **2021**, *121*, 1623–1669. [[CrossRef](#)] [[PubMed](#)]
- Hidrue, M.K.; Parsons, G.R.; Kempton, W.; Gardner, M.P. Willingness to pay for electric vehicles and their attributes. *Resour. Energy Econ.* **2011**, *33*, 686–705. [[CrossRef](#)]
- IEA. Key World Energy Statistics. Available online: <https://www.iea.org/events/key-world-energy-statistics-2018> (accessed on 21 February 2022).
- Cabana, J.; Monconduit, L.; Larcher, D.; Palacín, M.R. Beyond intercalation-based Li-ion batteries: The state of the art and challenges of electrode materials reacting through conversion reactions. *Adv. Mater.* **2010**, *22*, E170–E192. [[CrossRef](#)]
- Inagaki, M.; Toyoda, M.; Soneda, Y.; Morishita, T. Nitrogen-doped carbon materials. *Carbon* **2018**, *132*, 104–140. [[CrossRef](#)]
- Zheng, F.; Yang, Y.; Chen, Q. High lithium anodic performance of highly nitrogen-doped porous carbon prepared from a metal-organic framework. *Nat. Commun.* **2014**, *5*, 5261.
- Yasin, G.; Arif, M.; Ma, J.; Ibraheem, S.; Yu, D.; Zhang, L. Self-templating synthesis of heteroatom-doped large-scalable carbon anodes for high-performance lithium-ion batteries. *Inorg. Chem. Front.* **2022**, *9*, 1058–1069. [[CrossRef](#)]
- Xu, J.-S.; Zhu, Y.-J. Monodisperse Fe_3O_4 and $\gamma\text{-Fe}_2\text{O}_3$ magnetic mesoporous microspheres as anode materials for lithium-ion batteries. *ACS Appl. Mater. Interfaces* **2012**, *4*, 4752–4757. [[CrossRef](#)]
- Zhu, Q.; Chen, N.; Tao, F.; Pan, Q.M. Improving the lithium storage properties of $\text{Fe}_2\text{O}_3@\text{C}$ nanoparticles by superoleophilic and superhydrophobic polysiloxane coatings. *J. Mater. Chem.* **2012**, *22*, 15894–15900. [[CrossRef](#)]
- Nuli, Y.N.; Zhang, P.; Guo, Z.P.; Liu, H.K. Shape evolution of $\alpha\text{-Fe}_2\text{O}_3$ and its size-dependent electrochemical properties for lithium-ion batteries. *J. Electrochem. Soc.* **2008**, *55*, A196–A200. [[CrossRef](#)]
- Xua, Y.; Jianb, G.; Liua, Y.; Zhua, Y.; Zachariaha, M.R.; Wang, C. Superior electrochemical performance and structure evolution of mesoporous Fe_2O_3 anodes for lithium-ion batteries. *Nano Energy* **2014**, *3*, 26–35. [[CrossRef](#)]
- Larcher, D.; Masquelier, C.; Bonnin, D.; Chabre, Y.; Masson, V.; Lerche, J.-B.; Tarascon, J.-M. Effect of particle size on lithium intercalation into $\alpha\text{-Fe}_2\text{O}_3$. *J. Electrochem. Soc.* **2003**, *150*, A133–A139. [[CrossRef](#)]
- Liu, X.; Si, W.; Zhang, J.; Sun, X.; Deng, J.; Baunack, S.; Oswald, S.; Liu, L.; Yan, C.; Schmidt, O.G. Free-standing Fe_2O_3 nanomembranes enabling ultra-long cycling life and high rate capability for Li-ion batteries. *Sci. Rep.* **2014**, *4*, 7452. [[CrossRef](#)] [[PubMed](#)]

16. Balakrishnan, N.T.M.; Das, A.; Jishnu, N.S.; Krishnan, M.A.; Thomas, S.; Fatima, M.J.J.; Ahn, J.-H.; Prasanth, R. Electrospun nanostructured iron oxides for high-performance lithium ion batteries. In *Electrospinning for Advanced ENERGY Storage Applications*; in book Materials Horizons: From Nature to Nanomaterials; Balakrishnan, N.T.M., Prasanth, R., Eds.; Springer: Singapore, 2021; pp. 277–318.
17. Lin, Y.-M.; Abel, P.R.; Heller, A.; Mullins, C.B. α -Fe₂O₃ nanorods as anode material for lithium ion batteries. *J. Phys. Chem. Lett.* **2011**, *2*, 2885–2889. [[CrossRef](#)]
18. Yin, L.H.; Gao, Y.J.; Jeon, I.; Yang, H.; Kim, J.-P.; Jeong, S.-Y.; Cho, C.-R. Rice-panicle-like γ -Fe₂O₃@C nanofibers as high-rate anodes for superior lithium-ion batteries. *Chem. Eng. J.* **2019**, *356*, 60–68. [[CrossRef](#)]
19. Pham-Cong, D.; Kim, S.J.; Jeong, S.Y.; Kim, J.-P.; Kim, H.G.; Braun, P.V.; Cho, C.-R. Enhanced cycle stability of iron(II, III) oxide nanoparticles encapsulated with nitrogen-doped carbon and graphene frameworks for lithium battery anodes. *Carbon* **2018**, *129*, 621–630. [[CrossRef](#)]
20. Reis, G.S.D.; Oliveira, H.P.D.; Larsson, S.H.; Thyrel, M.; Lima, E.C.A. short review on the electrochemical performance of hierarchical and nitrogen-doped activated biocarbon-based electrodes for supercapacitors. *Nanomaterials* **2021**, *11*, 424. [[CrossRef](#)]
21. Li, H.Q.; Zhou, H.S. Enhancing the performances of Li-ion batteries by carbon-coating: Present and future. *Chem. Commun.* **2012**, *48*, 1201–1217. [[CrossRef](#)]
22. Aricò, A.S.; Bruce, P.; Scrosati, B.; Tarascon, J.-M.; Schalkwijk, W.V. Nanostructured materials for advanced energy conversion and storage devices. *Nat. Mater.* **2005**, *4*, 366–377. [[CrossRef](#)]
23. Wang, Y.; Cao, G. Developments in nanostructured cathode materials for high-performance lithium-ion batteries. *Adv. Mater.* **2008**, *20*, 2251–2269. [[CrossRef](#)]
24. Zheng, Z.M.; Li, P.; Huang, J.; Liu, H.; Zao, Y.; Hu, Z.; Zhang, L.; Chen, H.; Wang, M.-S.; Peng, D.-L.; et al. High performance columnar-like Fe₂O₃@carbon composite anode via yolk@shell structural design. *J. Energy. Chem.* **2020**, *41*, 126–134. [[CrossRef](#)]
25. Jung, S.-K.; Hwang, I.; Chang, D.H.; Park, K.-Y.; Kim, S.J.; Seong, W.M.; Eum, D.; Park, J.; Kim, B.; Kim, J.; et al. Nanoscale phenomena in lithium-ion batteries. *Chem. Rev.* **2020**, *120*, 6684–6737. [[CrossRef](#)] [[PubMed](#)]
26. Wang, J.; Liao, L.; Lee, H.R.; Shi, F.; Huang, W.; Zhao, J.; Pei, A.; Tang, J.; Zheng, X.; Chen, W.; et al. Surface-engineered mesoporous silicon microparticles as high-coulombic-efficiency anodes for lithium-ion batteries. *Nano Energy* **2019**, *61*, 404–410. [[CrossRef](#)]
27. Zhang, H.; Noh, W.Y.; Li, F.; Kim, J.H.; Jeong, H.Y.; Lee, J.S. Three birds, one-stone strategy for hybrid microwave synthesis of Ta and Sn codoped Fe₂O₃@FeTaO₄ nanorods for photo-electrochemical water oxidation. *Adv. Funct. Mater.* **2019**, *29*, 1805737. [[CrossRef](#)]
28. Zhang, C.; Chen, Z.; Wang, H.; Nie, Y.; Yan, J. Porous Fe₂O₃ nanoparticles as lithium-ion battery anode materials. *ACS Appl. Nano Mater.* **2021**, *4*, 8744–8752. [[CrossRef](#)]
29. Narsimulu, D.; Nagaraju, G.; Sekhar, S.C.; Ramulu, B.; Hussain, S.K.; Yu, J.S. Unveiling multi-channelled 3D porous iron oxide nanostructures with exalted capacity towards high-performance Li-ion battery applications. *J. Alloys Compd.* **2020**, *846*, 156385. [[CrossRef](#)]
30. Liu, D.; Shadique, Z.; Lin, R.; Qian, K.; Li, H.; Li, K.; Wang, S.; Yu, Q.; Liu, M.; Ganapathy, S.; et al. Review of recent development of in situ/operando characterization techniques for lithium battery research. *Adv. Mater.* **2019**, *31*, 1806620. [[CrossRef](#)]
31. Ghimire, P.C.; Bjattari, A.; Lim, T.M.; Wai, N.; Kazacos, M.S.; Yan, Q. *In-situ* tools used in vanadium redox flow battery research—Review. *Batteries* **2021**, *7*, 53. [[CrossRef](#)]
32. Su, Q.; Xie, D.; Zhang, J.; Du, G.; Xu, B. In situ transmission electron microscopy observation of the conversion mechanism of Fe₂O₃/graphene anode during lithiation–delithiation processes. *ACS Nano* **2013**, *7*, 9115–9121. [[CrossRef](#)]
33. Lee, K.; Shin, S.; Degen, T.; Lee, W.; Yoon, Y.S. In situ analysis of SnO₂/Fe₂O₃/RGO to unravel the structural collapse mechanism and enhanced electrical conductivity for lithium-ion batteries. *Nano Energy* **2017**, *32*, 397–407. [[CrossRef](#)]
34. Long, Z.; Yuan, L.; Shi, C.; Wu, C.; Qiao, H.; Wang, K. Porous Fe₂O₃ nanorod-decorated hollow carbon nanofibers for high-rate lithium storage. *Adv. Compos. Hybrid. Mater.* **2022**, *5*, 370–382. [[CrossRef](#)]
35. Chen, Z.; Dang, J.; Hu, X.; Yan, H. Reduction kinetics of hematite powder in hydrogen atmosphere at moderate temperatures. *Metals* **2018**, *8*, 751. [[CrossRef](#)]
36. Martin, T.P.; Merlin, R.; Huffman, D.R.; Cardona, M. Resonant two magnon Raman scattering in α -Fe₂O₃. *Solid State Commun.* **1977**, *22*, 565–567. [[CrossRef](#)]
37. Liu, J.; Liang, C.; Zhang, H.; Zhang, S.; Tian, Z. Silicon-doped hematite nanosheets with superlattice structure. *Chem. Commun.* **2011**, *47*, 8040–8042. [[CrossRef](#)]
38. Wang, L.; Yang, H.; Liu, X.; Zeng, R.; Li, M.; Hu, X. Constructing hierachial tectorum-like α -Fe₂O₃/PPy nanoarrays on carbon cloth for solid-state asymmetric supercapacitors. *Angew. Chem. Int. Ed.* **2017**, *56*, 1105–1110. [[CrossRef](#)]
39. Li, J.; Wang, Y.W.; Xu, W.N.; Wang, Y.; Zhang, B.; Luo, S.; Zhou, X.Y.; Zhang, C.L.; Gu, X.; Hu, C.G. Porous Fe₂O₃ nanospheres anchored on activated carbon cloth for high-performance symmetric supercapacitors. *Nano Energy* **2019**, *57*, 379–387. [[CrossRef](#)]
40. Cho, J.S.; Hong, Y.J.; Kang, Y.C. Design and synthesis of bubble-nanorod-structured Fe₂O₃–carbon nanofibers as advanced anode material for li-ion batteries. *ACS Nano* **2015**, *9*, 4026–4035. [[CrossRef](#)]
41. Chaudhari, S.; Srinivansan, M. 1D hollow α -Fe₂O₃ electrospun nanofibers as high performance anode material for lithium ion batteries. *J. Mater. Chem.* **2012**, *22*, 23049–23056. [[CrossRef](#)]

42. Chen, D.; Ji, G.; Ma, Y.; Lee, J.Y.; Lu, J. Graphene-encapsulated hollow Fe_3O_4 nanoparticle aggregates as a high-performance anode material for lithium ion batteries. *Appl. Mater. Interfaces* **2011**, *3*, 3078–3083. [[CrossRef](#)]
43. Aravindan, V.; Lee, Y.-S.; Madhavi, S. Best practices for mitigating irreversible capacity loss of negative electrodes in Li-ion batteries. *Adv. Energy Mater.* **2017**, *7*, 1602607. [[CrossRef](#)]
44. Guo, W.X.; Sun, W.; Lv, L.-P.; Kong, S.; Wang, Y. Microwave-assisted morphology evolution of Fe-based metal–organic frameworks and their derived Fe_2O_3 nanostructures for Li-ion storage. *ACS Nano* **2017**, *11*, 4198–4205. [[CrossRef](#)] [[PubMed](#)]
45. Xin, Q.; Gai, L.G.; Wang, Y.; Ma, W.Y.; Jiang, H.H.; Tian, Y. Hierarchically structured $\text{Fe}_3\text{O}_4/\text{C}$ nanosheets for Effective lithium-ion storage. *J. Alloys Compd.* **2017**, *691*, 592–599. [[CrossRef](#)]
46. Wu, Q.; Zhao, R.F.; Zhang, X.E.; Li, W.L.; Xu, R.H.; Diao, G.W.; Chen, M. Synthesis of flexible $\text{Fe}_3\text{O}_4/\text{C}$ nanofibers with buffering volume expansion performance and their application in lithium-ion batteries. *J. Power Sources* **2017**, *359*, 7–16. [[CrossRef](#)]
47. He, Z.; Wang, K.; Zhu, S.; Huang, L.-A.; Chen, M.; Guo, J.; Pei, S.; Shao, H.; Wang, J. MOF-derived hierarchical MnO-doped $\text{Fe}_3\text{O}_4/\text{C}$ composite nanospheres with enhanced lithium storage. *ACS Appl. Mater. Interfaces* **2018**, *10*, 10974–10985. [[CrossRef](#)]
48. Dong, Y.C.; Md, K.; Chui, Y.S.; Xia, Y.; Cao, C.W.; Lee, J.M.; Zapien, J.A. Synthesis of CNT@ $\text{Fe}_3\text{O}_4/\text{C}$ hybrid nanocables as anode materials with enhanced electrochemical performance for lithium ion batteries. *Electrochim. Acta* **2015**, *176*, 1332–1337. [[CrossRef](#)]
49. Jiang, H.; Huang, L.; Wei, Y.; Wang, B.; Wu, H.; Zhang, Y.; Liu, H.; Duo, S. Bio-derived hierarchical multicore–shell Fe_2N -nanoparticle-impregnated N-doped carbon nanofiber bundles: A host material for lithium-/potassium-ion storage. *Nano-Micro Lett.* **2019**, *11*, 56. [[CrossRef](#)]
50. Reddy, M.V.; Ting, Y.; Sow, C.-H.; Shen, Z.X.; Lim, C.T.; Rao, G.V.S.; Chowdari, B.V.R. α - Fe_2O_3 nanoflakes as an anode material for Li-ion batteries. *Adv. Funct. Mater.* **2007**, *17*, 2792–2799. [[CrossRef](#)]
51. Shin, H.C.; Cho, W.I.; Jang, H. Electrochemical properties of the carbon-coated LiFePO_4 as a cathode material for lithium-ion secondary batteries. *J. Power Sources* **2006**, *159*, 1383–1388. [[CrossRef](#)]
52. Reddy, M.V.; Madahavi, S.; Rao, G.V.S.; Chowdari, B.V.R. Metal oxyfluorides TiOF_2 and NbO_2F as anodes for Li-ion batteries. *J. Power Sources* **2006**, *162*, 1312–1321. [[CrossRef](#)]
53. Drach, Z.; Herskovitz, S.; Ferrero, D.; Leone, P.; Lanzini, A.; Santarelli, M.; Tsur, Y. Impedance spectroscopy analysis inspired by evolutionary programming as a diagnostic tool for SOEC and SOFC. *Solid State Ion.* **2016**, *288*, 307–310. [[CrossRef](#)]
54. Lai, L.-H.; Gomulya, W.; Protesescu, L.; Kovalenko, M.V.; Loi, M.A. High performance photoelectrochemical hydrogen generation and solar cells with a double type II heterojunction. *Phys. Chem. Chem. Phys.* **2014**, *16*, 7531–7537. [[CrossRef](#)] [[PubMed](#)]
55. Zhang, S.L.; Pan, N. Supercapacitors performance evaluation. *Adv. Energy Mater.* **2015**, *5*, 1401401. [[CrossRef](#)]
56. Nakamura, M.; Sato, N.; Hoshi, N.; Sakata, O. Outer helmholtz plane of the electrical double layer formed at the solid electrode–liquid interface. *Chem. Phys. Chem.* **2011**, *12*, 1430–1434. [[CrossRef](#)] [[PubMed](#)]
57. Schiclein, H.; Müller, A.C.; Voigts, M.; Krügel, A.; Ivers-Tiffée, E. Deconvolution of electrochemical impedance spectra for the identification of electrode reaction mechanisms in solid oxide fuel cells. *J. Appl. Electrochem.* **2002**, *32*, 875–882. [[CrossRef](#)]
58. Illig, J.; Ender, M.; Chrobak, T.; Schmidt, J.; Klotz, D.; Ivers-Tiffée, E. Separation of charge transfer and contact resistance in LiFePO_4 -cathodes by impedance modeling. *J. Electrochem. Soc.* **2012**, *159*, A952–A960. [[CrossRef](#)]
59. Schmidt, J.; Berg, P.; Schönleber, M.; Weber, A.; Ivers-Tiffée, E. The distribution of relaxation times as basis for generalized time-domain models for Li-ion batteries. *J. Power Sources* **2013**, *221*, 70–77. [[CrossRef](#)]
60. Michael, A.D. Generalized distribution of relaxation times analysis for the characterization of impedance spectra. *Batteries* **2019**, *5*, 53.
61. Bisquert, J.; Fabregat-Santiago, F.; Mora-Seró, I.; Garcia-Belmonte, G.; Giménez, S. Electron lifetime in dye-sensitized solar cells: Theory and interpretation of measurements. *J. Phys. Chem. C* **2009**, *113*, 17278–17290. [[CrossRef](#)]
62. Lian, C.; Gao, M.; Pan, H.; Liu, Y.; Yan, M. Lithium alloys and metal oxides as high-capacity anode materials for lithium-ion batteries. *J. Alloys Compd.* **2013**, *575*, 246–256. [[CrossRef](#)]
63. Lörger, S.; Usiskin, R.E.; Maier, J. Transport and charge carrier chemistry in lithium oxide. *J. Electrochem. Soc.* **2019**, *166*, A2215–A2220. [[CrossRef](#)]